

# A Bayesian Time-Varying Psychophysiological Interaction (PPI) Model for functional connectivity

Jaylen Lee<sup>1</sup>, Brian Schetzsle<sup>1</sup>, Aaron Bornstein<sup>2</sup>, Babak Shahbaba<sup>1</sup>, and Michele Guindani<sup>3</sup>

<sup>1</sup>Department of Statistics, University of California, Irvine

<sup>2</sup>Department of Cognitive Sciences, University of California,  
Irvine

<sup>3</sup>Department of Biostatistics, University of California, Los  
Angeles

## Abstract

Psychophysiological interaction (PPI) models have been largely employed to study task-modulated *seed-based* brain connectivity in fMRI studies. However, popular implementations of the PPI framework assume that the partial correlation between the seed region and the ROIs is static in the absence of a stimulus, whereas current developments in neuroimaging suggest that functional connectivity is by nature dynamic. In this paper, we propose a Bayesian modeling framework that extends the generalized PPI model and estimates task-modulated time-varying background functional connectivity from an fMRI experiment. In order to model the dynamics of the background regression coefficients, the framework employs a time-varying scale-mixture shrinkage prior that enforces sparsity of the non-zero coefficients. The approach is computationally efficient since it can be parallelized to identify functional connectivity patterns for different choices of the seed region. Then, the significant partial correlations across runs are selected by using a non-marginal decision-theory-based

multicomparison framework, which also leads to reduced spurious non-zero PPI effects. The performance of the model is illustrated in a simulation analysis and in an application to data from a serial reaction time experiment.

## 1 Introduction

In brain imaging, the study of functional connectivity (FC) using fMRI data has led to a better understanding of brain mechanisms, including how the brain responds to external stimuli. Those advances have also resulted in improved diagnoses and classifications of disease severity (Lynall et al., 2010; Anderson and Cohen, 2013, see, e.g.). Friston (2011) defines FC as the study of the (undirected) statistical dependencies between brain regions.

Psychophysiological interaction (PPI) models have been proposed by Friston et al. (1997) to study task-modulated *seed-based* brain connectivity in fMRI studies. More in detail, in task-based fMRI, it is of interest to investigate the effect modification of external stimuli (called *psychological* variables of the task design) onto the association between a seed region and other regions of interest (ROIs; also called *physiological* variables). From a statistical perspective, the PPI model typically takes the form of a linear regression model, where the BOLD signal of the seed region is assumed to be an additive linear function of the BOLD time series of other ROIs plus an interaction term, which captures the effect modification of the task via a product of the ROI times series and the stimulus function. If the coefficient of an interaction term is significantly different from zero, after taking into account the main effects of all the psychological and physiological variables, then we can conclude there is a task-dependent connectivity between the two brain regions. The original model by Friston et al. (1997) considered a single task condition. More recently, (McLaren et al., 2012) have proposed a *generalized PPI* approach that includes interaction effects for more than two conditions. Their framework directly models each task condition with respect to all other conditions in the regression framework. The PPI effects are then compared between the conditions of interest after the fit, rather than as in the original formulation by Friston et al. (1997), where the contrast information was used to define a psychological regressor.

In this paper, we propose a Bayesian characterization of the generalized PPI model in McLaren et al. (2012) and we further extend it in two signifi-

cant directions. On the one hand, popular implementations of the PPI model assume that the partial correlation between the seed region and the ROIs is static in the absence of a stimulus. However, current developments in neuroimaging suggest that FC is dynamic, that is the coupling between brain regions may be better characterized by *time-varying* levels of correlated or mutually informed activity (Iraji et al., 2019; Calhoun et al., 2014). Therefore, our first contribution is to extend the generalized PPI model to include a *dynamic process* which allows estimating task-modulated time-varying background FC during the course of an fMRI experiment. Our framework is designed to characterize time-varying FC that results from both task-related and spontaneous fluctuations in neural activity over time. In order to model the dynamics of the background regression coefficients, we use a time-varying scale-mixture shrinkage prior that has been proposed for variable selection in sparse Bayesian state-space models.

Seed-based FC analysis investigates the association of the fMRI signal from specific regions and the fMRI signals from any other region in the brain. The seed region is often selected based on the available prior literature or a testable research hypothesis. The primary benefit of seed analysis is that typically both the calculation and the interpretation of the neuroscientific findings are straightforward. However, if the seed region changes, the results may vary; hence, the choice of seed regions can impact the reproducibility and generalizability of the findings (Lv et al., 2018). One potential solution is to rotate the seed regions across the brain and create separate PPI models for each seed. However, testing for non-zero PPI effects in this context is guaranteed to find spurious non-zero PPI effects due to the high false positive rate. A Bonferroni correction will also be far too conservative, making it difficult to detect true correlations and PPI effects.

Our second contribution is to develop a new method for identifying significant associations between brain regions, which does not depend on the choice of a seed region. First, separate PPI models are run with each ROI serving as the seed region. This task is computationally efficient because it can be parallelized among many computer nodes. We then aggregate findings from each model and identify any significant partial correlations by adapting a non-marginal decision-theory-based multicomparison framework (Chandra and Bhattacharya, 2019). This multiple testing procedure is designed to control the rate of false positive decisions while still allowing the model to detect true non-zero correlations between regions.

The rest of the paper proceeds as follows. In Section 2, we introduce

the proposed time-varying PPI model. The shrinkage-inducing priors for the time-varying coefficients are described in Section 2.1. Section 3 describes how to obtain posterior inference from the Bayesian model, and Section 3.2 details the multicomparison procedure for combining inference across multiple seed-based analysis. The performance of the model is illustrated in a simulation analysis (Section 4) and an application to data from a serial reaction time experiment (Section 5). Finally, Section 6 concludes with a discussion of our proposed method, as well as plans for future investigation.

## 2 A Time-Varying PPI Model.

In this section, we introduce the proposed Bayesian time-varying PPI model, which considers the fMRI signal of a specific time-series for a region of interest as the outcome. This region is assumed to be the seed region. In our application, we run the model by varying the choice of seed region across all ROIs in the brain, and then we synthesize the results of the inference via the multicomparison procedure described in Section 3.2. Here, we describe the model for the BOLD signal of a generic seed ROI. We assume that we have fMRI time-series data from  $R$  ROIs across the brain, and we let  $Y_r(t)$  be the observed BOLD signal for a seed ROI,  $r \in \{1, \dots, R\}$ , observed at time points  $t = 1, \dots, T$ . In accordance with the PPI framework, we collect the BOLD signals of all ROIs except for the seed region  $r$  into a vector  $\mathbf{Z}_t^r = \{Y_d(t)\}_{d \neq r}$ , of dimension  $R - 1$ .

The bold signal  $Y_r(t)$  can be seen as a noisy realization of a convolution of the underlying neural signal,  $y_r(t)$ , and the hemodynamic response function (hrf),  $h_r(t)$ ,

$$Y_r(t) = \int_{-\infty}^t h_r(\tau) y_r(t - \tau) d\tau. \quad (1)$$

For the purpose of this paper, we assume a canonical hemodynamic response function, i.e. the hrf is defined as the difference of two gamma functions (Lindquist et al., 2009). The latent neural signals  $y_r(\cdot)$ ,  $r = 1, \dots, R$ , can be obtained from the deconvolution of the observed BOLD signal with the assumed hrf, using either the Weiner deconvolution (Wu et al., 2013) or latent feature encoding (Bush and Cisler, 2013).

Our proposed time-varying psychophysiological interaction (dPPI) model posits that the observed BOLD signal in region  $r$  is a function of dynamically

changing associations with all the other ROIs. These associations can be further affected by the observed stimulus. Let  $s_k(t)$  denote a stimulus function (more generally, a psychological variable of the task design) at time  $t$ , with  $k = 1, \dots, K$ , where  $K$  is a positive integer denoting the total number of stimuli in the task-based fMRI experiment. Then, the scalar-valued time series  $S_k(t) = \int_{-\infty}^t h(t) s_k(t-\tau) d\tau$  is the convolution of the stimulus  $k$  with the canonical hrf, for  $k = 1, \dots, K$ . We further define the  $(R - 1)$ -dimensional vector of time-series  $\mathbf{X}_k(t)$ , with entries

$$X_{kd}(t) = \int_{-\infty}^t h(t) s_k(t-\tau) y_d(t-\tau) d\tau, \quad d = 1, \dots, R, d \neq r,$$

capturing the psychophysiological interactions as the product of the neural signal of each ROI  $d$ ,  $d \neq r$ , with the stimulus  $k$ , convolved with the canonical hrf (see, e.g., Di et al., 2021). The vector  $\mathbf{Z}^r(t)$  denotes the  $(R - 1)$ -dimensional vector of the BOLD signals recorded at time  $t$  in all other ROIs, i.e., excluding ROI  $r$ . Then, we assume

$$Y_r(t) = \mathbf{Z}^r(t)^T \boldsymbol{\beta}^r(t) + \sum_{k=1}^K \{S_k(t) \alpha_k^r + \mathbf{X}_k(t)^T \boldsymbol{\gamma}_k^r\} + \epsilon_r(t), \quad (2)$$

where the scalar  $\alpha_k^r \in \mathbb{R}$  and the vector  $\boldsymbol{\gamma}_k^r \in \mathbb{R}^{R-1}$  denote the psychological and psychophysiological interaction effects for stimulus  $k$ ,  $k = 1, \dots, K$ , respectively, and the  $(R - 1)$ -dimensional vector  $\boldsymbol{\beta}^r(t)$  indicates the time-varying physiological effect capturing the FC between the seed region and any other region, independently of any stimulus effect. This effect can be regarded as capturing time-varying *baseline* FC, whereas the vector  $\boldsymbol{\gamma}_k^r \in \mathbb{R}^{R-1}$  captures how FC changes because of stimulus  $k$ . For simplicity, in the following, we will refer to (2) as the time-varying Psychophysiological interaction (tvPPI) model.

The proposed model effectively extends the Generalized PPI model of McLaren et al. (2012) by allowing the physiological effects, i.e., the correlation between ROIs, to change over time. Indeed, if  $\boldsymbol{\beta}^r(t) = \boldsymbol{\beta}$ , i.e. if the elements of  $\boldsymbol{\beta}^r(t)$  are constant over time, then the proposed tvPPI model reduces to the Generalized PPI model. Figure 1 provides an illustrative example of the type of time-varying relationship between two time series that the proposed model can help capture. We generate data from a centered bi-variate Gaussian process with marginal variance 1, and we assume that

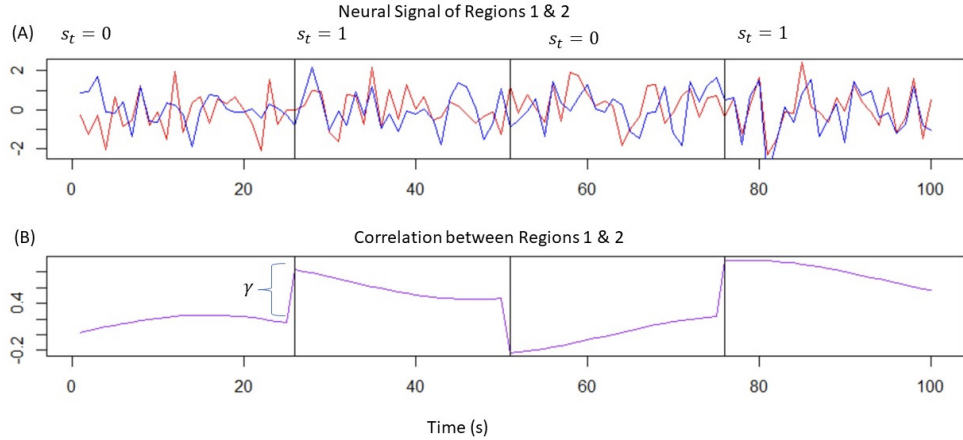


Figure 1: *Illustration of the proposed time-varying PPI paradigm (simulated time series)*: similarly to the Generalized PPI model, our proposed approach allows to capture stronger dependence between two realized time-series due to stimulus effects (top). In addition, it allows capturing smooth changes in the correlation over time, independent of the stimulus effect (bottom), whereby the generalized PPI model only allows constant effects over time. For more details on the Simulation setup, see Section 2.

the correlation between the realizations at each time  $t$  varies over time, according to the function  $\rho(t) = 0.2 \sin(t/10) + s(t)\gamma$ , where the task stimulus indicator  $s(t)$  switches between 0 and 1 every 25 seconds and  $\gamma = 0.6$  is the coefficient capturing the stimulus effect.

The two simulated time series in the displayed realization of Figure 1 (top) are only weakly dependent when  $s(t)$ , the task indicator, is equal to 0. The dependence increases and the time series are more strongly coupled when  $s(t) = 1$ . The PPI  $\gamma$  effect of the simulated stimulus  $s(t)$  is shown by the sudden jump when the stimulus becomes active in Figure 1 (bottom). However, the correlation between the two time series changes over time and slowly weakens the longer the block remains active. The smooth changes of the correlation over time are modeled by  $\beta(t)$ . The existing non-dynamic versions of PPI models are incapable of capturing the subtle fluctuations in the strength of connectivity between the two time-series.

We can use the partial correlation between region  $r$  and any other ROI  $d$  as a measure of functional connectivity. According to model (2), the partial

correlation between two regions is proportional to the direct effect of one region on the seed region, plus the interaction effects due to the stimuli,

$$\rho(r, d, t) \propto \beta_d^r(t) + \sum_{k=1}^K X_{kd}(t) \gamma_{kd}^r, \quad d = 1, \dots, R, d \neq r, \quad (3)$$

where  $\gamma_{kd}^r$  denotes the element of  $\boldsymbol{\gamma}_k^r$  corresponding to  $X_{kd}$ ,  $d = 1, \dots, R$ ,  $d \neq r$ .

By allowing the seed region to vary, we can fit  $R$  versions of the model and obtain partial correlations for any pair of regions at each time point. We can construct FC matrices at each time point, say  $P_t \in \mathcal{R}^{R \times R}$ ,  $t = 1, \dots, T$ , where the seed regions indicate the row number, the diagonal elements are ones and each off-diagonal term is the partial correlation for the associated seed region-ROI pair. The resulting FC matrices are not necessarily symmetric. More importantly, a significant partial correlation between  $r$  and  $d$ ,  $\rho(r, d, t)$  – with  $r$  assumed as seed region – does not guarantee that the partial correlation between  $d$  and  $r$ ,  $\rho(d, r, t)$  – with  $d$  assumed as seed region – is also significant. In Section 3.2, we describe a multi-comparison procedure to control the rate of false positive connectivities and regularize the inference across model fits.

## 2.1 Shrinkage Prior for the time-varying Physiological Effects

The time-varying coefficients in the vector  $\boldsymbol{\beta}^r(\mathbf{t})$  capture the relevant psychological effects between the seed region  $r$  and any other ROI  $d$ ,  $d = 1, \dots, R$ ,  $d \neq r$ . At any given time  $t$ , it is reasonable to expect that only a subset of the ROIs will be associated with the seed region. We use variable selection priors to regularize the inference problem and identify relevant associations between the BOLD signals. Recently, several Bayesian approaches have been proposed for dynamic variable selection priors in sparse time-varying state-space models (see, e.g., Rockova and McAlinn, 2020; Kowal et al., 2019). Here, we use the double gamma prior, which was recently proposed by Bitto and Frühwirth-Schnatter (2019) and Cadonna et al. (2020). This prior generalizes the popular Horseshoe prior (Carvalho et al., 2010) to the time-varying modeling framework. In our experience, this choice of prior is efficient from a computational perspective, helps to avoid overfitting by effectively shrinking

the variances of the time-varying coefficients to zero, and is flexible enough to adapt to varying degrees of sparsity in the data.

More in detail, the double gamma prior assumes that the psychological effect,  $\beta_d^r(t)$ , between a seed region  $r$  and an ROI  $d$  changes over time according to a discrete random walk,

$$\beta_d(t) = \beta_d(t-1) + w_d(t), \quad (4)$$

where we have dropped the superscript of the seed region,  $r$ , on the parameters for ease of notation. The step size  $w_d(t)$  is a random variable that follows a scale-mixture normal-gamma-gamma shrinkage prior on the variance components. This means that the variance of  $w_d(t)$  is governed by two gamma-distributed variables, one of which is itself a shrinkage-prior,

$$\begin{aligned} w_d(t) &\sim N(0, \theta_d), \\ \theta_d | \zeta_d &\sim G\left(\frac{1}{2}, \frac{1}{2\zeta_d}\right), \\ \zeta_d | a_\zeta \kappa_B &\sim G(a_\zeta, \frac{a_\zeta \kappa_B}{2}). \end{aligned} \quad (5)$$

The model specification included an initial condition, which assumes that at time  $t = 0$ ,  $\beta(0)_d \sim N(0, \theta_d)$ . This construction emphasizes the role of  $\theta_d$  in both identifying significant connectivities and determining whether or not those connections vary over time. A very small value of  $\theta_d$  encourages smooth transitions over time and coefficients that approach static (i.e., not time-varying) values. In particular, the coefficient  $\beta(0)_d$  should remain close to 0 over the entire time domain if it is initially close to 0, due to the small step size of the random walk process. The process prior (5) is an example of a *global-local* shrinkage prior: the parameter  $\kappa_B$  is a global shrinkage parameter that controls the overall level of sparsity among all the  $\theta_d$ 's,  $d = 1, \dots, R$ ,  $d \neq r$ . The parameter  $\zeta_d$  can be thought of as a local shrinkage parameter, since it allows shrinking the corresponding  $\theta_d$  to 0 as necessary. This has the effect of ensuring that non-zero  $\theta_d$  values do not decrease toward 0. The prior specification (4)–(5) depends on two hyperparameters:  $a_\zeta$  and  $\kappa_B$ . We follow Cadonna et al. (2020) and use a default of  $a_\zeta = 0.1$ , while we let  $\kappa_B$  be user-defined. A simulation of the double gamma prior distribution can provide information about the level of global shrinkage for specific values of  $\kappa_B$ . Figure 2 shows such a simulation. The conditional distribution of  $\theta | \zeta$  is heteroskedastic, with both increasing mean and variance as a function of  $\zeta$ .

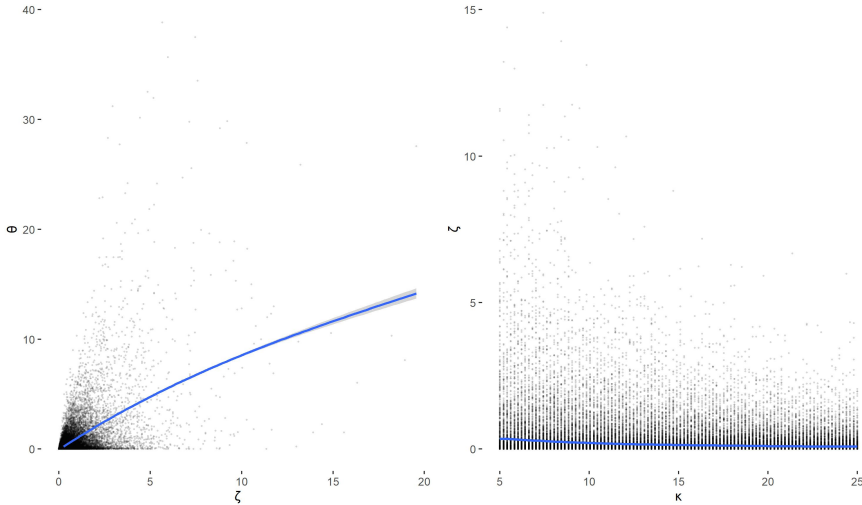


Figure 2: *Choice of the global shrinkage parameter  $\kappa_B$ :* Simulations from  $P(\theta|\zeta)$  where the blue line is a smoother estimating  $E(\theta|\xi)$  (left) and from  $P(\zeta|\kappa_B, a_\zeta = 0.1)$  (right) in (5). The conditional distribution of  $\theta|\zeta$  is heteroskedastic with increasing mean and variance as a function of  $\zeta$ . Larger and more varying values of  $\zeta$  are associated with smaller values of  $\kappa_B$ .

As  $\zeta$  increases,  $\kappa_B$  decreases. Setting  $\kappa_B$  to be large results in more sparse solutions, which are characterized by less dynamic changes in the coefficients. Setting  $\kappa_B$  to be small would correspond to preferring less sparse solutions *a priori*. Recently, Knaus et al. (2021) have suggested  $\kappa_B = 20$  as a default setting, which has been shown to exhibit good simulation performance.

## 2.2 Shrinkage Prior for the PPI Effects.

Model (2) includes  $K \times (R - 1)$  static psychophysiological interaction vectors,  $\boldsymbol{\gamma}_k^r = \{\gamma_{dk}\}_{d \neq r}$ , and  $K$  psychological effects,  $\alpha_k$ . We expect that only a sparse subset of the parameters will identify significant associations between the fMRI BOLD signal in the seed region and either the psychological or the PPI factors. Thus, we adopt the horseshoe prior of Carvalho et al. (2010) to shrink the irrelevant PPI and psychological effects to zero. More specifically, for notational simplicity, we introduce the vector  $\boldsymbol{\eta}_k = [\gamma_{1k}, \dots, \gamma_{R-1,k}, \alpha_k]$  to indicate the  $R$  dimensional vector concatenating the PPI and psychological effects of each stimulus  $k$ . We let  $\eta_{kh}$  denote the generic element of such

vector,  $k = 1, \dots, K$ ,  $h = 1, \dots, R$ . Then, we assume a global-local shrinkage prior for the coefficients,

$$\begin{aligned}\eta_{kh} | \tau^2, \lambda_{kh}^2 &\sim N(0, \tau^2 \lambda_{kh}^2), \quad h = 1, \dots, R, \\ \tau^2 &\sim C_+(0, 1), \\ \lambda_{kh}^2 &\stackrel{\text{ind}}{\sim} C_+(0, 1), \quad h = 1, \dots, R.\end{aligned}\tag{6}$$

where the parameters  $\tau$  and  $\lambda$  induce global and local shrinkage, respectively, of the coefficients toward zero. Here, the interest is in identifying the main effects and the interaction effects of psychophysiological factor on brain activity. These effects are assumed as static, i.e. not-time varying in order to maintain identifiability of all the model parameters. Indeed, if the stimuli are  $k$  blocked indicators – as is often the case – it would be challenging to learn the dependence structure between time-varying interaction parameters, say  $\gamma_{kd}(t)$  and  $\gamma_{kd}(t+1)$ , when  $s_k(t) = s_k(t+1) = 0$ . Given that we lack detailed prior information about how the connection between seed region  $r$  and region  $d$  is modified by successive exposures to stimulus  $k$ , choosing a static specification for these parameters allows us to make more easily interpretable inferences and reduces computational complexity.

### 3 Posterior Inference

In this Section, we outline how to obtain inference on the parameters of model (2). We first discuss the computational algorithm for drawing posterior samples of the parameters of interest, namely  $\alpha_k$ ,  $\beta_{dk}(t)$ , and  $\gamma_{dk}$ . The use of continuous global-local shrinkage priors for the model parameters does not ensure that the posterior distribution of irrelevant parameters will have positive probability mass at *exact zero*. Therefore, we propose a selection procedure inspired by the work of Chandra and Bhattacharya (2019) on testing the related hypotheses. By casting the selection problem in a *non-marginal* multi-comparison framework, our approach is able to combine inferences from different models that assume different seed-regions, and obtain unique connection graphs. Lastly, we discuss constructing point estimates for the time varying partial correlation matrices  $P_t \in \mathcal{R}^{R \times R}$ ,  $t = 1, \dots, T$ .

### 3.1 Markov Chain Monte Carlo Algorithm

Posterior inference for each seed-region is conducted in parallel through Markov Chain Monte Carlo (MCMC). In the following, we discuss the implementation for a single seed-region, say  $r \in \{1, \dots, R\}$ , as in equation (2). The choice of prior distributions described in the previous section allows simulation from the joint posterior of the parameters by combining the collapsed sampler employed by Cadonna et al. (2020) for the time-varying regression coefficients  $\beta_d(t)$  and the auxiliary variable augmented Gibbs sampler of Makalic and Schmidt (2016) for the static regression coefficients  $\eta_k$ . The general procedure for sampling the parameters is straightforward and computationally efficient. Once all parameters are initialized, we simply iterate between the following two steps:

1. **Update**  $\beta, \theta, \zeta, \sigma$  : Let  $Y_\beta(t) = Y(t) - \sum_{k=1}^K \mathbf{X}_{tk}^T \boldsymbol{\gamma}_k, \forall t$ . Then follow steps A-D of Algorithm 1 in Cadonna et al. (2020).
2. **Update**  $\eta, \tau, \lambda$  : Let  $Y_\gamma(t) = Y(t) - \mathbf{Z}^r(t)^T \boldsymbol{\beta}_t, \forall t$ . Use the conditional distributions in Makalic and Schmidt (2016) equations 7 and 8, by substituting  $\eta$  for  $\beta$  in their notation.

The first step is efficiently implemented in R using the *shrinkTVP* package by Knaus et al. (2021). Once again, it is worth noting that since the model specified in Equations 2–6 is independent across each seed region, we can fit each of the  $R$  models in parallel leading to a sizeable computational gain.

### 3.2 Selection of Non-Zero Components

In the Bayesian literature, variable selection is often implemented either by using continuous shrinkage priors or discrete selection models, e.g. through a spike-and-slab prior specification (George and McCulloch, 1993, 1997). The latter approach explicitly allows computing the posterior probability that a coefficient is exactly zero, but imposes additional computational complexity. Although continuous shrinkage priors result in increased computational speed, they lack generally accepted selection criteria and require careful posterior assessment of the inference. For example, Carvalho et al. (2010) as well as Cadonna et al. (2020) suggest using a thresholding approach on the estimated values of a latent shrinkage factor to identify relevant coefficients.

The problem at hand presents two sets of challenges that make conventional thresholding approaches difficult to apply directly. On the one hand, at each time point  $t = 1, \dots, T$ , the lack of connectivity between the seed region  $r$  and any other region  $d$  should be assessed by testing the statement:  $H_{0rdt} : \beta_d^r(t) + \sum_{k=1}^K X_{kd}(t)\gamma_{kd}^r = 0$ , which encodes conditional independence between the two regions by setting the corresponding partial correlations to zero. Any post-MCMC selection procedure that is used to infer the coefficients of a model should take into account both the static and time-varying coefficients of the model. Indeed, Cadonna et al. (2020) apply a thresholding rule on a local shrinkage factor which tests the relevance of the coefficient  $\sqrt{\theta_d}$  in (5). However, this solution cannot be applied to our hypothesis of interest due to the way  $\theta_d$  affects not just which variables are included, but also whether  $\beta_{td}$  is time-varying or not.

A second important consideration is that decisions based on a model studying the association between seed region  $d$  and all the other brain regions should take into account also the inference for models that assume any other brain region as seed region. In other words, when testing for the null hypothesis  $H_{0rdt} : \beta_d^r(t) + \sum_{k=1}^K X_{kd}(t)\gamma_{kd}^r = 0$ , where  $r$  is the seed region, it is desirable for the results to agree with the corresponding test of  $H_{0drt}$  where  $d$  is the seed region. Maintaining this consistency would ensure that FC remains non-directed. We are faced with a multi-comparison problem with dependent hypotheses when we consider the combined results of all models obtained by rotating the seed-regions.

We adapt the non-marginal decision theoretic approach recently developed by Chandra and Bhattacharya (2019) in order to identify relevant FC associations. Here, the word non-marginal means that the decision theoretical framework does not rely solely upon marginal decision rules, e.g., marginal distributions of the test statistics, marginal p-values or marginal posterior probabilities, as is often the case for standard multi-comparison procedures. Instead, the framework in Chandra and Bhattacharya (2019) allows for the incorporation of the joint structure inherent in hypotheses and the dependence between parameters directly in the error measures. As a result, the approach leads to a modified false discovery rate (mFDR) criterion that is more accurate than marginal methods.

In more detail, let  $G_{rdt} = \{H_{0rdt}, H_{1rdt}, H_{0drt}, H_{1drt}\}$  denote the collection of null and alternative hypotheses statements for identifying the association between regions  $r$  and  $d$ . The alternative hypothesis when  $r$  is the seed-region can be described as  $H_{1rdt} : \beta_d^r(t) + \sum_{k=1}^K X_{kd}(t)\gamma_{kd}^r \neq 0$  for every  $d \neq r$ ,

$d, r = 1, \dots, R$ , and similarly for  $H_{1drt}$ . Let the function the function  $D_{rdt} = I(H_{1rdt} \text{ is accepted})$  indicate the decision in favor of conditional dependence (non-null FC) between regions  $r$  and  $d$  at time  $t$ , if region  $r$  is the seed ROI. Correspondingly, let  $z_{rdt} = I(H_{1drt} \text{ is accepted})$  indicate the decision in support of FC between  $d$  and  $r$  at time  $t$ , if region  $d$  is the seed ROI. Lastly, let  $h_{rdt}$  indicate the true state of nature, i.e. if  $r$  and  $d$  are functionally connected ( $h_{rdt} = 1$ ) or not ( $h_{rdt} = 0$ ). Let  $\mathcal{A}_t$  denote the set of triplets  $(r, d, t)$  formed as we vary  $r, d = 1, \dots, R, r \neq d$ , at a given  $t, t = 1, \dots, T$ . Following Chandra and Bhattacharya (2019), at each time  $t = 1, \dots, T$ , a non-marginal decision rule will aim at maximizing the posterior expectation of true positive decisions (TP):

$$TP_t = \sum_{i \in \mathcal{A}_t} D_i h_i z_i$$

while controlling for possible decision errors.  $TP_t$  denotes the number of cases for which both  $H_{1drt}$  and  $H_{1rdt}$  are correctly accepted. In the context of non-marginal decision rules, errors may derive from the fact that related hypotheses are wrongly accepted, wrongly rejected, or the decisions are not coherent with each other. Chandra and Bhattacharya (2019) show that these errors add up to the following cumulative sum,

$$E = \sum_{i \in \mathcal{A}_t} D_i (1 - h_i z_i). \quad (7)$$

The resulting loss function can be seen as a constrained maximization of the posterior expectation of positive decisions penalized by both making false positive decisions as well as non-symmetric decisions. Thus, the objective function can be rewritten as a function of the admissible decisions in the set of all possible decision configurations, under some penalization constant  $\eta \in \mathbb{R}^+$ :

$$f_\eta(\mathbf{D}) = \sum_{i \in \mathcal{A}_t} D_i (w_i(\mathbf{D}) - \eta), \quad (8)$$

where for any given triplet  $(r, d, t)$  in  $\mathcal{A}_t$ ,  $w_{rdt}(\mathbf{D}) = P(H_{1rdt} \cap H_{1drt} | Y)$  denotes the posterior of the joint probability of the alternative hypotheses capturing the FC between regions  $r$  and  $d$ . All the models are fit separately across all seed regions. Thus, we can compute  $w_{rdt}(\mathbf{D})$  as the product of the

two tail probabilities,

$$w_{rdt}(\mathbf{D}) = P \left( |\beta_d^r(t) + \sum_{k=1}^K X_{kd}(t) \gamma_{kd}^r| \geq c\sigma^r \right) P \left( |\beta_r^d(t) + \sum_{k=1}^K X_{kr} \gamma_{kr}^d| \geq c\sigma^d \right)$$

for some small  $c \in \mathcal{R}$ . In all the following implementations, we have seen that  $c = 0.1$  suffices to obtain good operating characteristics.

Chandra and Bhattacharya (2019) suggest a multi-step approach to maximize the objective function (8). First, they set the penalization constant  $\eta = 1 - mFDR_x$ , where the  $mFDR_x \in (0, 1)$  indicates the *posterior modified false discovery rate* and is a measure of Type-I error in multiple testing. More in detail, the  $mFDR_x$  is defined as

$$mFDR_x = \sum_{\mathbf{D} \in \mathcal{D}} \frac{\sum_{i \in \mathcal{A}_t} D_i (1 - w_i(\mathbf{D}))}{\sum_i D_i} \delta(\mathbf{D} | \mathbf{Y}), \quad (9)$$

where  $\mathcal{D}$  denotes the space of all possible decision configurations, and the indicator variable  $\delta(\mathbf{D} | \mathbf{Y})$  is equal to one for the final decision.

Chandra and Bhattacharya (2019) use a simulated annealing method to maximize  $f_\eta(\mathbf{D})$ , for each given  $\eta$ . However, the posterior of  $mFDR_x$  encodes an additional penalty for the incorrect decisions, particularly when the weights  $w_{rdt}$  are small. Thus, using the  $mFDR_x$  to define the penalty may lead to an overly conservative procedure. As a way around the problem, they propose running the simulated annealing algorithm multiple times, progressively decreasing  $\eta$  until the desired  $mFDR_x$  is achieved; however, this approach is computationally burdensome for large datasets. Here, we employ an alternate approach, which has been motivated by the following realization. In our experiments, the achieved  $mFDR_x$  is often below the nominal false discovery rate when the initial run of the simulated annealing algorithm leads to optimal decision pairs that are discordant, i.e. of the type  $D_{rdt} \neq D_{drt}$ ,  $r, d = 1, \dots, D$ . Subsequent runs of annealing algorithms tend to reduce these discrepancies. Therefore, in order to gain computational speed, after the run of the simulated annealing algorithm, all the decisions are inspected and we conclude that two regions are *not* associated only if the optimal solution identified by the annealing algorithms sets both  $D_{rdt} & D_{drt} = 0$ . This simple modification is computationally efficient and appears to perform well in our investigations.

### 3.3 Inference on Partial Correlations

Utilizing the non-marginal decision rules and our modified algorithm, we can then estimate the level of correlation between pairs of regions. Specifically, we use the posterior samples from the MCMC algorithm to estimate physiological and PPI effects, leading to the construction of time-varying precision matrices  $\Omega_{rt} \in \mathcal{R}^{R \times R}, t = 1, \dots, T$ , where the subscript  $r$  denotes a given seed region  $r$ ,  $r = 1, \dots, R$ .

Since model (2) assumes Gaussianity, conditional independence can be evaluated by looking at the distribution of  $Y_r(t)$  conditioned on all other regions  $Z_r(t)$ ,

$$Y_r(t) | Z^r(t) \sim N \left( -\frac{\Omega_{rz^r t}}{\Omega_{rrt}} Z^r(t), \Omega_{rrt}^{-1} \right), \quad (10)$$

where  $\Omega_{rrt}$  is a scalar, corresponding to the  $r^{th}$  diagonal entry of  $\Omega_t$ , the index  $z^r$  briefly indicates all the regions except the seed region,  $r$ , and  $\Omega_{rz^r t}$  is a vector of partial correlations, the  $r^{th}$  row of  $\Omega_t$ , excluding the entry on the diagonal. Comparing with (2), it follows that  $\Omega_{rrt} = \text{Var}(\epsilon_t)^{-1}$ . The vector of partial correlations  $\Omega_{rz^r t}$  can be approximated by  $\Omega_{rz^r t} \approx \beta^r(t) + \sum_{k=1}^K X_{kd}(t) \gamma_k^r$ , after subtracting the psychological effects. Here, we assume that although the elements  $X_{kd}(t) = \int_{-\infty}^t h(t) s_k(t - \tau) y_d(t - \tau) d\tau$  of  $\mathbf{X}_k(t)$  do not coincide with  $S_k(t) Z_d^r(t)$ ,  $d = 1, \dots, R$ ,  $d \neq r$ , their values should be similar in a small neighborhood of each time point. Thus, using Equation (10) and the non-marginal decision theoretic approach outlined in Section 3.2, we can estimate the partial correlations from each fitted seed-based model, say  $\tilde{\Omega}_{rt}$ , from the posterior samples of  $\beta_t$ ,  $\gamma_k$  and  $\sigma_t^r$ . Then, we can combine the results across runs and obtain a final estimate of the time-varying precision matrix  $\hat{\Omega}_t$  by setting each off-diagonal entry as follows:

$$\hat{\Omega}_{rdt} = \begin{cases} 0 & \text{if } D_{rdt} \& D_{drt} = 0 \\ \frac{\tilde{\Omega}_{rdt} + \tilde{\Omega}_{drt}}{2} & \text{otherwise} \end{cases} \quad r, d = 1, \dots, R \quad (11)$$

where – for any two regions  $r$  and  $d$  – the decisions  $D_{rdt}$  and  $D_{drt}$  are the optimal decisions obtained by the simulated annealing algorithm of Chandra and Bhattacharya (2019) in the models fitted assuming seed region  $r$  and  $d$ , respectively. See Section 3.2.

## 4 Simulation

In this Section, we compare our proposed dPPI model with the standard generalized PPI (gPPI) of McLaren et al. (2012). In this setting, we show how the model performs when estimating PPI effects under an assumption of resting-state time-varying functional connectivity.

We simulate data from a Gaussian distribution with a time-varying covariance matrix where the PPI effects are known explicitly, so that we can compare the bias and standard errors of the PPI effects of interest. We simulate response time courses for  $R = 12$  regions over  $T = 600$  in an event related design, assuming  $K = 2$  stimuli. We then simulate data as  $Y(t) \sim N_{12}(0, (\Omega_{S(t)}^1)^{-1} + (\Omega_t^2)^{-1})$ , that is assuming that the time-varying partial correlations are the result of two additive covariance (precision) processes. The use of precision matrices allows us encoding of the conditional independences of the network. The first component is a stimulus linked process. The precision matrix is  $\Omega_{s(t)}^1$  where  $s(t) = 0, \dots, K$  is the stimulus sequence. Here,  $\Omega_0^1$  denotes the precision matrix during rest: it is assumed as block diagonal consisting of four  $3 \times 3$  matrices. In contrast,  $\Omega_1^1$ , the precision matrix when  $s(t) = 1$ , is equal to  $\Omega_0^1$  for the first and last  $3 \times 3$  block diagonal entries, while the middle  $6 \times 6$  block diagonal entries are modeled so to create a PPI effect under stimulus 1. In an analogous way,  $\Omega_2^1$  assumes that the middle  $6 \times 6$  block diagonal entries are equal to  $\Omega_0^1$ , but the first and last  $3 \times 3$  block matrices are modified. In this way, there are no PPI effects for the first 3 regions, while other regions have their connectivity modified by at least one stimulus. The second component is characterized by a precision process  $\Omega_t^2$ , which is fully time-varying and it is defined equal to the identity matrix except for the (1,2)-(2,1) entries and the (14,15)-(15,14) entries. For those entries, we set  $\Omega_t^2(1, 2) = \Omega_t^2(2, 1) = 0.43 \sin(\frac{0.01\pi t}{2} + 2.2)$  and  $\Omega_t^2(10, 11) = \Omega_t^2(11, 10) = 0.47 \sin(\frac{0.017\pi t}{2} - 1.3)$ . This characterization simulates a partial correlation between the region pairs which fluctuates regardless of the active stimulus. We create 60 simulated datasets to fit both the dPPI and generalized PPI models. We then construct partial correlation matrices  $\Omega_t^{dppi}$  and  $\Omega_t^{gppi}$  using the method outlined in Section 3.3.

To assess the performances of the two models, we compare the bias and standard errors of three PPI effects of interest. Using the notation of Equation 2, we focus on  $\gamma_{21}^1$ , i.e., the PPI between regions 1 and 2 with stimulus 1, and then  $\gamma_{51}^4$  and  $\gamma_{11,2}^{10}$ . Since  $\Omega_0^1(1, 2) = \Omega_1^1(1, 2)$ , we expect  $\gamma_{21}^1 = 0$  even

Method	$\gamma_{2,1}^1 = 0$	$\gamma_{5,1}^4 = -0.055$	$\gamma_{11,2}^{10} = 0.269$	MSE
gPPI	0.170 (0.088)	-0.076 (0.106)	0.101 (0.106)	240.231 (29.471)
dPPI	0.090 (0.097)	-0.062 (0.088)	0.210 (0.100)	188.546 (27.169)
dPPI w/ selection	0.073 (0.099)	-0.041 (0.125)	0.238 (0.122)	147.557 (26.033)

Table 1: The results of the comparison between the proposed dPPI and the general PPI model of McLaren et al. (2012) across 60 simulated datasets. Each column entry is the mean and standard deviation of the estimates of the chosen effect modifications across all simulations. The rows corresponds to proposed dPPI model, the results of the dPPI model after the dPPI selection procedure of Section 3.3 and the gPPI. The dPPI achieves less bias and lower MSEs under a setting where physiological effects are time-varying.

though there is a time-varying correlation between the two regions. Instead, we expect  $\gamma_{51}^4$  to be non-zero as the (4,5)-pair has a constant resting state correlation and a non-zero constant PPI with stimulus 1. Finally, we consider  $\gamma_{11,2}^{10}$  since the (10,11)-pair exhibits both a time-varying resting state correlation and a non-zero PPI with stimulus 2. The results are compiled in Table 1. The last column reports the mean squared errors, defined as  $MSE = \sum_{t=1}^T \sum_{r=2}^R \sum_{d=1}^r (\Omega_{rdt} - \hat{\Omega}_{rdt})^2$  for the true partial correlation matrix coefficients at time  $t$ ,  $\Omega_t$  and the estimate under each model,  $\hat{\Omega}_{rdt}$ . The dPPI and gPPI rows are simply the mean and standard deviations across simulation datasets for the PPI effects,  $\gamma$ , of interest. The dPPI w/ selection row computes the PPI effects after selection by computing the differences in the partial correlations when the simulated subject transitions from the rest condition to the stimulus condition of interest after the dPPI selection procedure of Section 3.3 has been applied. Overall, the dPPI exhibits less bias in estimating the partial correlations under a resting state time-varying functional connectivity model. This is especially true when considering the region pair (10,11) which has both a time-varying resting state partial correlation and a non-zero PPI with stimulus 2. The dPPI model also achieves lower MSE when estimating the partial correlation trajectories between all regions, since gPPI fails to capture changes in partial correlation that are independent of the stimuli considered. The selection is shown to have additional benefits by reducing both bias for the PPI effects and the MSE for the partial correlations among all regions.

Figure 3 shows the paths of the estimated partial correlations for the (1,2)-, (4,5)-, and (10,11)- region pairs from a single simulation dataset. The

dPPI is able to recover the underlying time-varying partial correlations while also accommodating the effects of stimulus 2, by modifying the partial correlations for the (1,2)- and (10,11)- region pairs. In addition, the second row, corresponding to the (4,5)-pair, shows that the dPPI is also able to perform similarly to the gPPI in the absence of resting state time-varying partial correlations, thus showing the benefits of the shrinkage prior on  $\beta_d(t)$ . Figure 4 (top) averages the time-indexed partial correlations over each rest/stimulus block for a single simulation dataset, outputting a form of static functional connectivity matrix. We see that our proposed selection procedure is able to recover the changes in the structure of the partial correlation matrix under each stimulus block.

## 5 Functional connectivity modulated by *look-ahead* predictions

A topic of continuing interest in cognitive neuroscience is how individuals learn predictive associative relationships that can be used to support decision-making and planning for rewards (Daw and Shohamy, 2008). Our interest lies in studying the modification of functional connectivity associations as a function of learning in a predictive learning experiment. More specifically, we have available data on eight subjects who were shown a probabilistic sequence of 4 images and were tasked with responding to the shown image with a matched pre-trained button press (Bornstein and Daw, 2012). The sequence of images were randomly generated (unknown to the participants) according to a first order Markov process, where the probability a picture is shown in trial  $e = 1, \dots, 999$ , depends solely on the picture shown in trial  $e-1$ . The transition matrix can be represented by a  $4 \times 4$  matrix, where each  $(i, j)$  entry specifies the probability that the picture identified by the  $j^{th}$  column entry is shown on trial  $e$  given that the picture identified by the  $i^{th}$  row is shown on trial  $e-1$ . To encourage continual learning, the Markov transition kernels were changed twice, at trials  $e = 334$  and  $e = 667$ . The participants' reaction times (RTs) were measured as a proxy for predictive learning - faster reaction times indicating that they had learned the conditional distribution of the image sequence. The transition matrices were generated anew for each subject, and selected to minimize mixing time. This was done so that first-order dependencies would be the only consistent source of information about

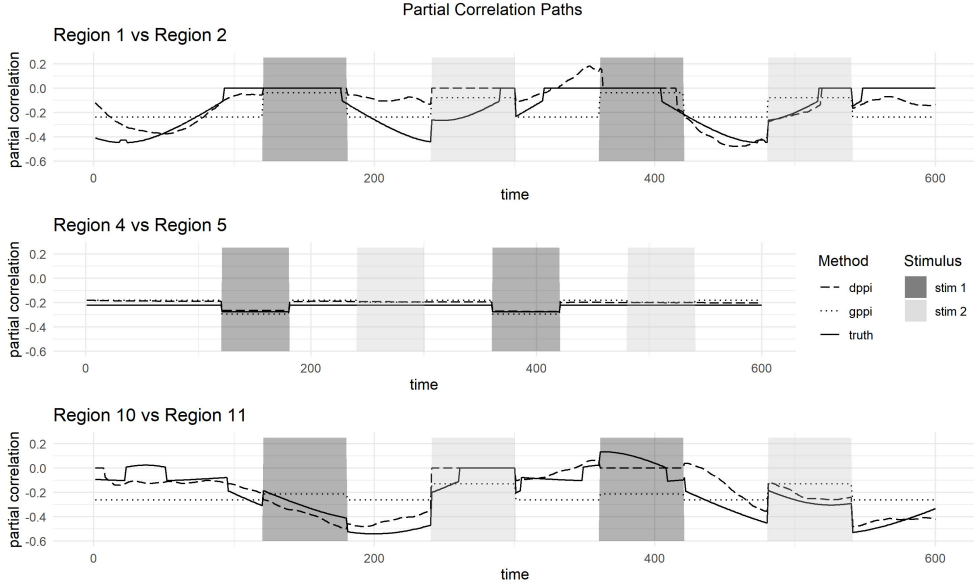


Figure 3: The paths of the estimated partial correlations for the (1,2)-, (4,5)-, and (10,11)- region pairs from a single simulation dataset. The solid black line shows the true partial correlations for the respective region pairs over time. The dashed and dotted lines are the estimates from the dPPI and gPPI models, respectively, constructed using the method outline in Section 3.3. The dPPI is able to recover the underlying time-varying correlations while also accommodating the effects of stimulus 2 modifying the partial correlations in the (1,2)- and (10,11)- region pairs. The (4,5)- region pair shows that the dPPI is also able to perform similarly to the gPPI in the absence of resting state time-varying partial correlations, showing the benefits of the shrinkage prior on  $\theta_d(t)$ .

the identity of the next stimulus, and could be used as the primary predictor of behavior.

## 5.1 Learning rules and estimation of the lookahead activity

The relationship between the RTs and the underlying stimulus probabilities is typically captured by the learning rate, which measures the weight a system (a subject) places on new information relative to previous expe-

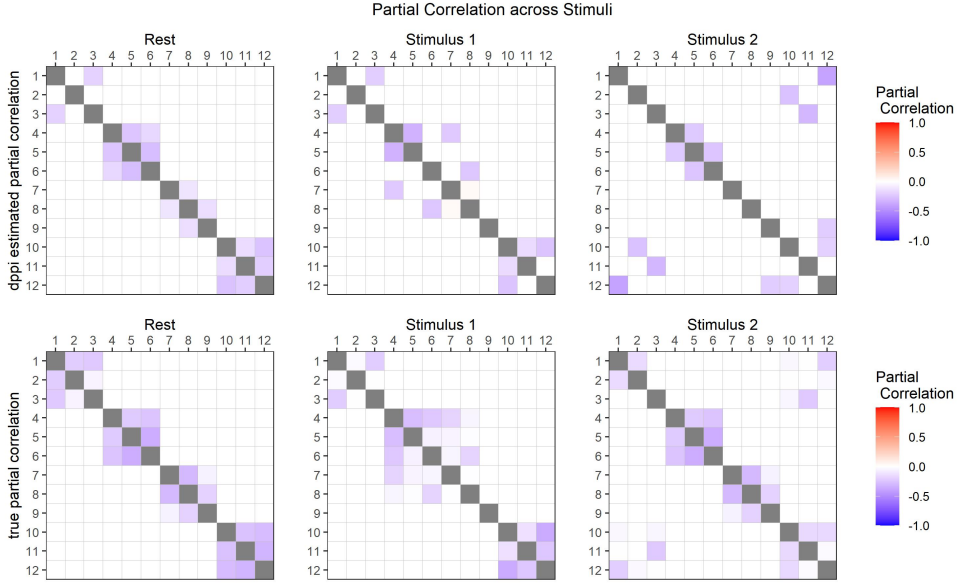


Figure 4: The average partial correlation matrices across each condition for a single simulation dataset. (Top row) The average estimated partial correlation matrices across the rest, stimulus 1, and stimulus 2 conditions respectively. (Bottom row) The average data-generating partial correlation matrices across the rest, stimulus 1, and stimulus 2 conditions respectively.

rience. Following previous work on the division of learning into multiple systems (Poldrack et al., 2001; Gläscher and Büchel, 2005), we consider two Rescorla-Wagner learning rules under an assumption of either a slow and a fast learning rate:  $P^s, P^f \in \mathcal{R}^{4 \times 4 \times 999}$ . These equations capture the participants' learned conditional distribution of the images according to each learning rate. More specifically, let  $I(e) \in \{1, 2, 3, 4\}$  indicate the label of the image shown at trial  $e = 1, \dots, 999$ . We compute the learning rules as

$$P_{i,j,e}^z = \begin{cases} P_{i,j,e-1}^z + \alpha_z(1 - P_{i,j,e-1}^z) & j = I(e) \\ P_{i,j,e-1}^z + \alpha_z(0 - P_{i,j,e-1}^z) & j \neq I(e) \end{cases} \quad z = s, f; \quad e = 1, \dots, 999, \quad (12)$$

where  $\alpha_s = 0.0138$  and  $\alpha_f = 0.5499$  are median parameter values across the population, estimated as in (Bornstein and Daw, 2012). We then use the learning rules (12) to compute the *forward entropy* of the system under the two learning rates, say  $H_s(e)$  and  $H_f(e)$  for the slow and fast rates,

respectively. The forward entropy is a measure of the expected surprise of the next image given the participant’s current experience and the image they are currently viewing, under an assumed learning rate. It captures the amount of *lookahead* activity to be expected in anticipation of the upcoming stimulus (Johnson and Redish, 2007; Bornstein and Daw, 2013):

$$H_z(e+1) = - \sum_{j=1}^4 \log(P_{I(e),j,e}^z) P_{I(e),j,e}^z \quad z = s, f. \quad (13)$$

Lookahead activity has been identified in several regions related to learning and memory, which suggests that these regions are involved in *predictions* as well (Johnson and Redish, 2007; Johnson et al., 2007). Since each region learns a different representation of sequential structure, and our behavior is a mix of the predictions generated by each representation, it remains an open question where and how these predictions are integrated (Daw and Shohamy, 2008). A key candidate structure is the Anterior Cingulate Cortex (ACC), a region that has the necessary anatomical connectivity to combine inputs from the hippocampal formation with those from the striatum, and which has itself been strongly associated with conflict between, and control of, competing motivational drives (Shenhav et al., 2013). Intuitively, if the brain represents sets of two or more competing predictions that can drive behavior, these predictions should be weighted according to their relative precision – here, the inverse of their entropy (Wang et al., 2022; Khoudary et al., 2022). Therefore, as the transition matrix representations change with learning, the more predictive representation should be more tightly coupled with ACC.

## 5.2 Time-varying psychophysiological interaction and lookahead activity

The proposed time-varying dPPI model allows us to test a question that is not possible to answer using standard methods. More specifically, we investigate whether the relationship between ACC and each “source” region (hippocampus and caudate) changes as a function of the difficulty of the task, measured by the lookahead (entropy) in each process. In other words, the goal is to estimate the PPI effect of the two forward entropy time series across the brain, with particular interest in the relationship between the two learning structures and ACC.

Imaging was performed on the 3T Siemens Allegra head only scanner with time resolution of 2.0 seconds per acquisition, across four sessions of 300 acquisitions each. Images were normalized into a template and resampled into  $2 \times 2 \times 2$ -mm voxels in the normalized template space (MNI). The voxels were then further combined into  $R = 18$  ROIs by taking the mean BOLD signal of all voxel time series attributed to each ROI. The ROIs were defined anatomically according to a standard atlas (AAL). The regions selected were structures previously associated with learning, memory, and decision-making, along with several “control” regions, and separated bilaterally. We consider  $K = 4$  covariates of interest in the model:

1. An indicator for the participant seeing an image
2. An indicator for the participant pressing a button
3. The forward entropy under the slow learning rate:  $H_s(\cdot)$
4. The forward entropy under the fast learning rate:  $H_f(\cdot)$

Each covariate was convolved with the canonical hrf, using the default implementation in the software SPM, to create the psychological regressors. PPI regressors were formed by first deconvolving the ROI time series into latent neural signals using the method of Bush and Cisler (2013), and then taking the product of the deconvolved time series with the four covariates above, before scaling and convolving once again with the canonical hrf (Di et al., 2017).

Consistent with the neural circuit model described above, our results show a consistent pattern of entropy-modulated time-varying PPIs between each source region and ACC. Specifically, we found that the functional connectivity between ACC and Caudate increases when the opposing (slow, hippocampally-linked) process becomes more uncertain (Figure 5, top panel). This pattern suggests that Caudate is more tightly coupled with activity in the putative output structure, ACC when hippocampus has greater difficulty predicting the next stimulus in the sequence. Notably, the observation that the predominance of Caudate depends on the predictiveness of the hippocampal representation, independent of the predictiveness of the Caudate representation itself, is consistent with an inductive bias towards the former structure, perhaps due to its faster neural dynamics and reflecting its more recency-weighted predictions (Wang et al., 2022).

Furthermore, we observed time-varying PPIs that suggested a role of each region in performing lookahead activity at the base of behavior. Specifically, as prediction becomes more difficult in the fast LR process, we find greater coupling between Caudate and Putamen (Figure 5, middle panel), a structure widely observed to represent the action sequences upon which the Caudate transition matrix may draw during lookahead (Smith and Graybiel, 2013). Paralleling the fast entropy-mediated Caudate-Putamen relationship, greater entropy in the slow (hippocampal) process was associated with stronger connectivity between hippocampus and parahippocampal cortex (Figure 5, bottom panel). The latter region is widely referred to as the *parahippocampal place area* (PPA; Epstein and Kanwisher, 1998) due to its sensitivity to the presentation and prospective imagination of complex “scene” images. Given that the stimuli in this experiment were images of natural scenes, this finding is consistent with the idea that, during lookahead, hippocampus is orchestrating reinstatements of scene images – as entropy increases, so does the number of potential next-step scene images that may be reinstated (see Bornstein and Daw, 2013; Bornstein and Norman, 2017, for corresponding findings in serial decision-making tasks).

## 6 Discussion

We have introduced a novel Bayesian model which is able to estimate PPI effects in the presence of possibly non-linear background time-varying functional connectivity. The method can be parallelized to separately consider multiple seed region across all ROIs in the brain, and then combines the results of multiple related linear models using a non-marginal decision framework that summarizes the inference into a single precision matrix and performs selection on the entries of the precision matrix, simultaneously adjusting for the multiplicity. In simulations, the proposed dPPI model exhibits less bias in estimating PPI effects when the time-varying changes in functional connectivity are not predicted by stimuli, and performs similarly to gPPI in estimating PPI effects of non-dynamically correlating regional pairs. In an application to a predictive learning experiemnt, our results show a consistent pattern of entropy-modulated time-varying PPIs between each Caudate, Putamen and ACC. While the proposed method allows sampling for each region’s parameters in parallel, a computational benefit, further extensions may consider simultaneous inference schemes that allow obtaining

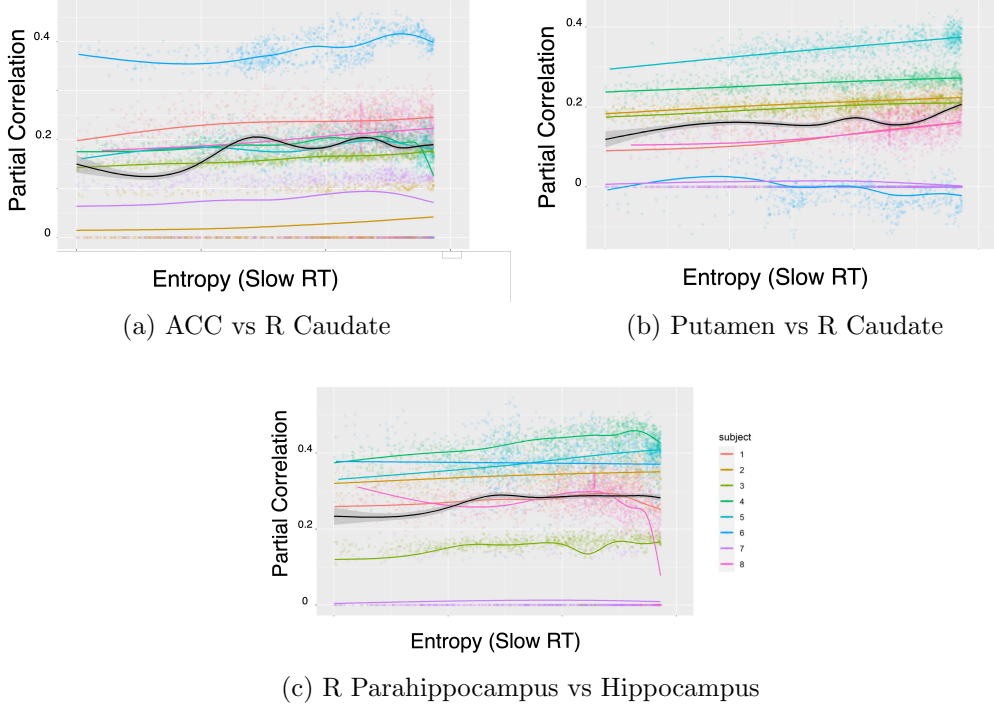


Figure 5: **Top:** The estimated time-varying partial correlations between the right side Caudate and ACC as a function of the time-varying entropy of the slow learning rate process. Each line corresponds to one of the eight subjects. **Middle:** The estimated partial correlation between right side Caudate and Putamen as a function of the time-varying entropy of the slow learning rate process. **Bottom:** The estimated partial correlation between right side Parahippocampus and the Hippocampus by the time-varying entropy of the slow learning rate process. See Sections 5.1 and 5.2 for details on the experiment and the analysis.

inference from PPI models from all seed regions in a single modeling framework. Such schemes could also include Bayesian nonparametric priors to perform model-based clustering of PPIs effects and functional connectivity patterns over time and subjects.

## **7 Acknowledgements**

The authors thank Nathaniel D. Daw for permission to re-analyze the functional MRI data.

## References

- Ariana Anderson and Mark S. Cohen. Decreased small-world functional network connectivity and clustering across resting state networks in schizophrenia: An fMRI classification tutorial. *Frontiers in Human Neuroscience*, 7(SEP):1–18, 2013. ISSN 16625161. doi: 10.3389/fnhum.2013.00520.
- Angela Bitto and Sylvia Frühwirth-Schnatter. Achieving shrinkage in a time-varying parameter model framework. *Journal of Econometrics*, 210(1):75–97, 2019. ISSN 0304-4076.
- Aaron M. Bornstein and Nathaniel D. Daw. Dissociating hippocampal and striatal contributions to sequential prediction learning. *European Journal of Neuroscience*, 35(7):1011–1023, 4 2012. ISSN 1460-9568. doi: 10.1111/j.1460-9568.2011.07920.X. URL <https://onlinelibrary.wiley.com/doi/full/10.1111/j.1460-9568.2011.07920.x>  
<https://onlinelibrary.wiley.com/doi/abs/10.1111/j.1460-9568.2011.07920.x>  
<https://onlinelibrary.wiley.com/doi/10.1111/j.1460-9568.2011.07920.x>.
- Aaron M Bornstein and Nathaniel D Daw. Cortical and hippocampal correlates of deliberation during model-based decisions for rewards in humans. *PLoS computational biology*, 9(12):e1003387, 2013.
- Aaron M Bornstein and Kenneth A Norman. Reinstated episodic context guides sampling-based decisions for reward. *Nature neuroscience*, 20(7):997–1003, 2017.
- Keith Bush and Josh Cisler. Decoding neural events from fMRI BOLD signal: A comparison of existing approaches and development of a new algorithm. *Magnetic Resonance Imaging*, 31(6):976–989, 7 2013. ISSN 0730725X. doi: 10.1016/j.mri.2013.03.015. URL <https://linkinghub.elsevier.com/retrieve/pii/S0730725X1300101X>.
- Annalisa Cadonna, Sylvia Frühwirth-Schnatter, and Peter Knaus. Triple the gamma—a unifying shrinkage prior for variance and variable selection in sparse state space and TVP models. *Econometrics*, 8(2):0–36, 2020. ISSN 22251146. doi: 10.3390/econometrics8020020.

Vince D. Calhoun, Robyn Miller, Godfrey Pearson, and Tulay Adali. The Chronnectome: Time-Varying Connectivity Networks as the Next Frontier in fMRI Data Discovery. *Neuron*, 84(2):262–274, 2014. ISSN 10974199. doi: 10.1016/j.neuron.2014.10.015.

Carlos M. Carvalho, Nicholas G. Polson, and James G. Scott. The horse-shoe estimator for sparse signals. *Biometrika*, 97(2):465–480, 2010. ISSN 00063444. doi: 10.1093/biomet/asq017.

Noirrit Kiran Chandra and Sourabh Bhattacharya. Non-marginal decisions: A novel bayesian multiple testing procedure. *Electronic Journal of Statistics*, 13(1):489–535, 2019. ISSN 19357524. doi: 10.1214/19-EJS1535.

Nathaniel D. Daw and Daphna Shohamy. The Cognitive Neuroscience of Motivation and Learning. *Social Cognition*, 26(5):593–620, 10 2008. ISSN 0278-016X. doi: 10.1521/soco.2008.26.5.593. URL <http://guilfordjournals.com/doi/10.1521/soco.2008.26.5.593>.

Xin Di, Richard C. Reynolds, and Bharat B. Biswal. Imperfect (de)convolution may introduce spurious psychophysiological interactions and how to avoid it. *Human Brain Mapping*, 38(4):1723–1740, 4 2017. ISSN 10659471. doi: 10.1002/hbm.23413. URL <https://onlinelibrary.wiley.com/doi/10.1002/hbm.23413>.

Xin Di, Zhiguo Zhang, and Bharat B. Biswal. Understanding psychophysiological interaction and its relations to beta series correlation. *Brain Imaging and Behavior*, 15(2):958–973, 2021.

Russell Epstein and Nancy Kanwisher. A cortical representation of the local visual environment. *Nature*, 392(6676):598–601, 1998.

K. J. Friston, C. Buechel, G.R Fink, J. Morris, E. Rolls, and J. Dolan. Psychophysiological and Modulatory Interactions in Neuroimaging. *NeuroImage*, 6(6):218–229, 1997. ISSN 10008055. URL <https://doi.org/10.1006/nimg.1997.0291>.

Karl J. Friston. Functional and Effective Connectivity: A Review. *Brain Connectivity*, 1(1):13–36, 2011. ISSN 2158-0014. doi: 10.1089/brain.2011.0008. URL <http://www.liebertonline.com/doi/abs/10.1089/brain.2011.0008>.

- Edward I. George and Robert E. McCulloch. Variable selection via Gibbs sampling. *Journal of the American Statistical Association*, 88(423):881–889, 1993. ISSN 1537274X. doi: 10.1080/01621459.1993.10476353. URL <http://www.jstor.org/stable/2290777?origin=crossref>.
- Edward I. George and Robert E. McCulloch. Approaches for bayesian variable selection. *Statistica Sinica*, 7(2):339–373, 1997. ISSN 10170405.
- Jan Gläscher and Christian Büchel. Formal learning theory dissociates brain regions with different temporal integration. *Neuron*, 47(2):295–306, 2005.
- Armin Iraji, Thomas P. Deramus, Noah Lewis, Maziar Yaesoubi, Julia M. Stephen, Erik Erhardt, Aysneil Belger, Judith M. Ford, Sarah McEwen, Daniel H. Mathalon, Bryon A. Mueller, Godfrey D. Pearlson, Steven G. Potkin, Adrian Preda, Jessica A. Turner, Jatin G. Vaidya, Theo G.M. van Erp, and Vince D. Calhoun. The spatial chronnectome reveals a dynamic interplay between functional segregation and integration. *Human Brain Mapping*, 40(10):3058–3077, 2019. ISSN 10970193. doi: 10.1002/hbm.24580.
- Adam Johnson and A David Redish. Neural ensembles in ca3 transiently encode paths forward of the animal at a decision point. *Journal of Neuroscience*, 27(45):12176–12189, 2007.
- Adam Johnson, Matthijs AA van der Meer, and A David Redish. Integrating hippocampus and striatum in decision-making. *Current opinion in neurobiology*, 17(6):692–697, 2007.
- Maria Khoudary, Megan AK Peters, and Aaron M Bornstein. Precision-weighted evidence integration predicts time-varying influence of memory on perceptual decisions. *Cognitive Computational Neuroscience*, 2022.
- Peter Knaus, Angela Bitto-Nemling, Annalisa Cadonna, and Sylvia Frühwirth-Schnatter. Shrinkage in the Time-Varying Parameter Model Framework Using the R Package shrinkTVP. *Journal of Statistical Software*, 100(13), 2021. ISSN 15487660. doi: 10.18637/JSS.V100.I13.
- Daniel R. Kowal, David S. Matteson, and David Ruppert. Dynamic shrinkage processes. *Journal of the Royal Statistical Society. Series B: Statistical Methodology*, 81(4):781–804, 2019. ISSN 14679868. doi: 10.1111/rssb.12325.

- Martin A. Lindquist, Ji Meng Loh, Lauren Y. Atlas, and Tor D. Wager. Modeling the hemodynamic response function in fmri: Efficiency, bias and mis-modeling. *NeuroImage*, 45(1, Supplement 1):S187–S198, 2009. ISSN 1053-8119. Mathematics in Brain Imaging.
- H. Lv, Z. Wang, E. Tong, L.M. Williams, G. Zaharchuk, M. Zeineh, A.N. Goldstein-Piekarski, T.M. Ball, C. Liao, and M. Wintermark. Resting-state functional mri: Everything that nonexperts have always wanted to know. *American Journal of Neuroradiology*, 39(8):1390–1399, 2018. ISSN 0195-6108.
- Mary-ellen Lynall, Danielle S Bassett, Robert Kerwin, Peter J Mckenna, Ulrich Müller, and Ed Bullmore. Functional connectivity and brain networks in schizophrenia. *Journal of Neuroscience*, 30(28):9477–9487, 2010. ISSN 1529-2401. doi: 10.1523/JNEUROSCI.0333-10.2010.Functional.
- Enes Makalic and Daniel F. Schmidt. A simple sampler for the horseshoe estimator. *IEEE Signal Processing Letters*, 23(1):179–182, 2016. ISSN 10709908. doi: 10.1109/LSP.2015.2503725.
- Donald G. McLaren, Michele L. Ries, Guofan Xu, and Sterling C. Johnson. A generalized form of context-dependent psychophysiological interactions (gPPI): A comparison to standard approaches. *NeuroImage*, 61(4):1277–1286, 2012. ISSN 10538119. doi: 10.1016/j.neuroimage.2012.03.068. URL <http://dx.doi.org/10.1016/j.neuroimage.2012.03.068>.
- Russell A Poldrack, Jill Clark, EJet al Paré-Blagoev, Daphna Shohamy, J Crespo Moyano, Catherine Myers, and Mark A Gluck. Interactive memory systems in the human brain. *Nature*, 414(6863):546–550, 2001.
- Veronika Rockova and Kenichiro McAlinn. Dynamic Variable Selection with Spike-and-Slab Process Priors. *Bayesian Analysis*, 16(1):233–269, 2020. ISSN 19316690. doi: 10.1214/20-BA1199.
- Amitai Shenhav, Matthew M Botvinick, and Jonathan D Cohen. The expected value of control: an integrative theory of anterior cingulate cortex function. *Neuron*, 79(2):217–240, 2013.
- Kyle S Smith and Ann M Graybiel. A dual operator view of habitual behavior reflecting cortical and striatal dynamics. *Neuron*, 79(2):361–374, 2013.

Shaoming Wang, Samuel F Feng, and Aaron M Bornstein. Mixing memory and desire: How memory reactivation supports deliberative decision-making. *Wiley Interdisciplinary Reviews: Cognitive Science*, 13(2):e1581, 2022.

Guo Rong Wu, Wei Liao, Sebastiano Stramaglia, Ju Rong Ding, Huafu Chen, and Daniele Marinazzo. A blind deconvolution approach to recover effective connectivity brain networks from resting state fMRI data. *Medical Image Analysis*, 17(3):365–374, 2013. ISSN 13618415. doi: 10.1016/j.media.2013.01.003. URL <http://dx.doi.org/10.1016/j.media.2013.01.003>.